Self-organization in unstable thin liquid films: dynamics and patterns in systems displaying a secondary minimum

Jayant Singh & Ashutosh Sharma

Self-organization in unstable thin liquid films: dynamics and patterns in systems displaying a secondary minimum

JAYANT SINGH and ASHUTOSH SHARMA *

Department of Chemical Engineering, Indian Institute of Technology, Kanpur 208 016, India

Abstract—Dynamics, stability, morphology, and dewetting of a thin film (< 100 nm) under the influence of a long-range van der Waals attraction combined with a short-range repulsion are studied based on numerical solutions of the nonlinear two-dimensional (2-D) thin film equation. Area and connectivity measures are used to analyze the morphology and the distinct pathways of evolution of the surface instability. The initial disturbance resolves into an undulating structure of uneven 'hills and valleys'. Thereafter, the morphology depends on the mean film thickness relative to the minimum of the force curve. Relatively thin films to the left of the minimum transform directly into an array of droplets via the fragmentation of ridges. At long times, the droplets merge due to ripening. In contrast, relatively thick films are dewetted by the formation and growth of isolated, circular holes. Coalescence of holes eventually leads to the formation of ridges and drops. Films of intermediate thickness display a rich combination of different morphologies. Thus, the morphology and the sequence of evolution depend crucially on the form of the potential and the film thickness relative to the location of the minimum in the force vs. thickness curve. Different types of patterns can, therefore, even co-exist on a heterogeneous surface.

Keywords: Thin films; dewetting; pattern formation; spinodal decomposition.

1. INTRODUCTION

Stability, dynamics, morphology, and adhesion failure by dewetting in thin films (< 100 nm) are of increasing concern in a host of technological and scientific settings such as coatings, flotation, emulsions, and physical and biological thin film phenomena (e.g. wetting, adhesion, colloid stability, biomembrane morphology).

It is now well understood [1–4] that the free surface of a thin film is unstable and deforms spontaneously whenever its disjoining pressure, engendered by the excess intermolecular interaction, increases with increasing local film thickness. In other words, instability by the 'spinodal decomposition' mechanism results whenever the

---

*To whom correspondence should be addressed. E-mail: ashutos@iitk.ac.in

spinodal parameter, defined as the second derivative of the free energy per unit area, is negative. The total free energy is the sum of its many possible components, the most prominent of which are the Lifshitz–van der Waals interactions (which include the dispersion and dipolar interactions), electrostatic interaction, and shorter-range acid–base, entropic, and structural interactions. In our nomenclature, an 'attractive' ('repulsive') component is one which engenders attraction (repulsion) between the two surfaces (interfaces) of the film.

Experiments [5–18] have shown that surface instability leads to a variety of microstructures in thin films, ranging from micro-droplets to holes, as well as a spectrum of bicontinuous undulating structures. However, theoretical understanding of self-organized thin film patterns and their relationship to intermolecular interactions have been rudimentary, and even deceptive, in so much as they are based largely either on the linear stability analysis [1, 2, 4, 19–23] or on one-dimensional (1-D) nonlinear analysis [19–22]. While these approaches have uncovered much of the underlying physics, they cannot be used to resolve the actual three-dimensional (3-D) morphologies and pathways of dewetting. The problem of 3-D nonlinear pattern selection has only recently been addressed based on the full 2-D nonlinear equation of evolution for thin films [24–26]. In particular, two distinct types of thin film systems have been studied, both of which display a lone primary minimum in the free energy close to the point of dewetting or pseudo-dewetting: (a) thin films subject to the Lifshitz–van der Waals attraction [24] and (b) thin films subject to a long-range van der Waals repulsion combined with a shorter range attraction [25, 26]. Films of system (a), regardless of their thickness, as well as relatively thick films of system (b), were found to dewet the substrate by the formation of isolated circular holes. Interestingly, in films of system (b), the morphological pathway of dewetting changed as the film thickness was reduced closer to the location of the minimum in the spinodal parameter. A decrease in the film thickness leads first to dewetting by an undulating bicontinuous pattern (rather than holes) and then by an array of isolated circular droplets. Thus, while a bicontinuous undulating pattern has usually been considered to be a hallmark of spinodal processes [1, 11–13, 27], nonlinear interactions can lead to a variety of other self-organizing patterns.

The main objective of this investigation was to uncover the variety of morphological patterns *on a homogeneous substrate* which can form spontaneously in an unstable film subject to the long-range van der Waals attraction combined with a short-range repulsion (these will be referred to as 'Type II' systems) and the conditions for the selection of a particular pattern. The combination of short- and long-range repulsive and attractive forces in thin films (as in flocculating colloids) usually leads to the existence of a secondary minimum in the free energy, disjoining pressure, and spinodal parameter isotherms. The long-range attraction is usually due to the Lifshitz–van der Waals interaction on nonwettable substrates [4, 20, 28, 29]. The shorter-range repulsion can be due to one or more of the following: van der Waals interaction with a thin wettable solid coating of the substrate [22], hydrophilic repulsion in aqueous films [28], electrical double-layer repulsion, and entropic effects

in adsorbed or grafted polymer films [14–16, 30, 31]. In other classes of interesting systems, the presence of a significant secondary (and even tertiary) minimum is engendered by the layering or ordering of repeat units, e.g. liquid crystals [18], films containing colloidal particles or surfactants [32, 33], block polymers, and organic multilayers [34].

The basic physics and 1-D nonlinear simulations for type II thin films are reported elsewhere [4, 20]. The growth of surface instability leads to (pseudo-) dewetting, and eventually to a quasistable structure consisting of a periodic array of cylindrical micro-drops in (quasi-) equilibrium with the intervening thin films. True dewetting or drying of the substrate does not occur since a relatively thick adsorbed flat film of thickness corresponding to the *secondary* minimum in the free energy is left behind. When the free energy per unit area displays both a primary minimum (molecularly close to the substrate) and a secondary minimum (at relatively large thickness), we use the term 'pseudo-dewetting' to signify that an equilibrium film of thickness close to the secondary minimum is left on the surface. The usual term 'dewetting', which conveys the idea of an almost dry surface, can be used when the equilibrium film left on the substrate corresponds to the primary minimum. Although both types of dewetting are seen in experiments on liquid-crystal films [18], spinodal dewetting of relatively thick films can lead only to pseudo-dewetting. True dewetting requires the overcoming of an energy barrier separating the primary and secondary minima, which may be possible by 'nucleation' induced by heterogeneities [18].

In this paper we address the problem of pattern selection, complete 3-D morphology, and morphological pathways of pseudo-dewetting for unstable type II films displaying a secondary minimum in the spinodal region. These issues are investigated based on numerical solutions of the nonlinear 2-D thin film equation. The simulations reported here provide a formalism for correlating the film morphology with the interfacial interactions and the film thickness, and will make it possible to compare theory and experiments directly in the future. Such a formalism will also help us to address the inverse problem of characterization of surface interactions from the observed morphology.

2. THEORY

We consider a thin (< 100 nm) Newtonian fluid film on a smooth, chemically homogeneous solid surface ($x-y$ plane). Evaporation and condensation are neglected, as is the case for high viscosity, low vapor pressure polymer films. The following nondimensional thin film equation [20, 24–26], derived from the Navier–Stokes equations, governs the stability and spatio-temporal evolution of a thin film subject to excess intermolecular interactions (where $\Phi_H = [2\pi h^2/|A|][\partial^2 \Delta G/\partial H^2]$, and A is the effective Hamaker constant):

$$\partial H/\partial T + \nabla \cdot \left[H^3 \nabla(\nabla^2 H) \right] - \nabla \cdot \left[H^3 \Phi_H \nabla H \right] = 0, \qquad (1)$$

where $H(X, Y, T)$ is the nondimensional local film thickness scaled with the mean thickness, h. The spatial coordinates, X, Y, in the plane of the substrate are scaled with the characteristic length scale for the van der Waals case [20], $(2\pi\gamma/|A|)^{1/2}h^2$. Nondimensional time, T, is scaled with $(12\pi^2\mu\gamma h^5/A^2)$, where γ and μ refer to the film surface or interfacial tension and viscosity, respectively. A renormalized real time, $t_N = t(A^2/12\pi^2\mu\gamma) = Th^5$, can also be defined to remove the influence of the mean film thickness. Finally, $\Phi_H = (2\pi h^4/|A|)(\partial^2\Delta G/\partial h^2)$ is the nondimensional spinodal parameter. ∇ is the usual 2-D gradient operator, $i(\partial/\partial X) + j(\partial/\partial Y)$. The rationale for this type of nondimensionalization is given elsewhere [20, 22].

The first term of the thin film equation denotes unsteady force (containing viscosity), which merely retards the growth of instability. The second term denotes the effect of surface tension for a curved surface, which in a 3-D geometry may be stabilizing (due to 'in-plane' curvature as in 2-D cases) or destabilizing (due to transverse curvature as in Rayleigh instability of circular cylinders). The third term describes the effect of excess intermolecular interactions, which engender instability by causing flow from thinner to thicker regions in the case of negative 'diffusivity', namely when the spinodal parameter $\Phi_H < 0$.

For simulations, we consider a fairly general excess intermolecular interaction free energy composed of a long-range (algebraic) attraction and a short-range (exponential) repulsion [4, 20–25, 29, 35], i.e.

$$\Delta G = -(A/12\pi h^2) + S^P \exp\left[(d_0 - h)/l_p\right], \qquad (2)$$

where d_0 (= 0.158 nm) is a molecular cut-off thickness [29], l_p is the decay length for the short-range repulsion and h is the film thickness. A is the effective Hamaker constant, which is positive (signifying long-range attraction) when the surface tensions for the substrate and the bounding medium are both either larger or smaller than that of the film material [4, 20, 22, 29]. S^P (> 0) measures the strength of the shorter-range non-van der Waals repulsion at the substrate surface at $h = d_0$. Qualitative variation of the spinodal parameter $\partial^2\Delta G/\partial h^2$ is as shown in Fig. 1 for two different sets of parameters. A different qualitative variation of the spinodal parameter results for type IV systems where the net van der Waals force is repulsive $(A < 0)$ and the shorter-range non-van der Waals forces are attractive $(S^P < 0)$. The morphology of type IV systems is considered elsewhere [25, 26].

While a convenient analytical representation for repulsion is chosen in equation (2) and realistic sets of parameters are chosen for illustration, the key features of morphology (e.g. whether a circular hole forms, etc.) and the pathways of evolution were found to be independent of these details. Based on our previous work [24–26] and a large number of additional simulations, we have verified that the distinct qualitative pathways of pattern evolution depend only on the qualitative *form* of the potential, rather than on its precise analytical representation. The key feature of the potential being investigated here is the presence of an unstable secondary spinodal region, which is separated from the primary spinodal region by
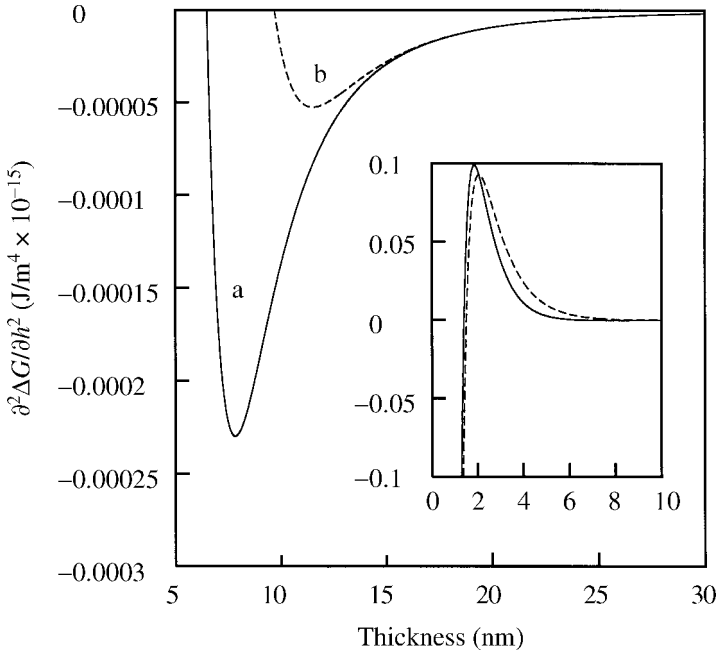
Figure 1. Variations of the spinodal parameter (force per unit volume, $[\partial^2 \Delta G/\partial h^2] \times 10^{-15}$) with the film thickness. Curve a: $A = 9.41 \times 10^{-21}$ J, $S^P = 1.2$ mJ/m^2, $l_p = 0.83$ nm. Curve b: $A = 9.41 \times 10^{-21}$ J, $S^P = 1.2$ mJ/m^2, $l_p = 1.1$ nm. The inset shows details for small thickness. Instability occurs for 1.39 nm $> h > 6.49$ nm for curve a and for 1.5 nm $> h > 9.7$ nm for curve b, where $\partial^2 \Delta G/\partial h^2 < 0$.

an intervening region where films are stable. The problem of pattern formation in the primary spinodal region has already been addressed [24–26]. Hence, we will confine attention to the self-organization around the secondary minimum.

The linear stability analysis [1–4, 20, 24] of the 3-D thin film equation (1) predicts a dominant nondimensional characteristic length scale of the instability $\lambda = 4\pi/\sqrt{-\Phi_H}$, which is the diagonal length of a unit square cell of length $L = \lambda/\sqrt{2}$.

In order to address the problem of pattern selection, we directly solved the nonlinear thin film equation numerically over an area of $9L^2$, starting with an initial small amplitude (≈ 1 Å) random perturbation. An ADI (alternating-direction implicit) technique was implemented, which combines the accuracy of an implicit integration scheme with the efficiency of an explicit scheme. Details of this numerical method can be found elsewhere [36, 37]. Briefly, over a single time step, all derivatives in one direction (say X) are discretized by an implicit scheme, and all derivatives in the other direction (Y), as well as the mixed derivatives, are discretized by an explicit scheme. At the next time step, the discretizing schemes in each direction are reversed. A 45×45 grid was usually found to be sufficient for convergence when central differencing in space with half-node interpolation

was combined with Gear's algorithm for time marching. The latter is a variable-order accurate method with automatic adjustment of time steps, which is especially suitable for stiff equations. Several simulations were also repeated for a 60×60 grid and some simulations were repeated over an area of $16L^2$ to rule out the influence of the grid density and the finite domain size on the result.

3. RESULTS AND DISCUSSION

We found two completely different sequences of evolution by which (pseudo) dewetting could occur, depending on the distance between the mean film thickness and the location of the minimum in the spinodal parameter. All of the simulations reported below are for the system represented by curve a of Fig. 1, unless otherwise noted.

Figure 2 summarizes the major events in the time evolution of patterns in a 7 nm thick film (which lies to the left of the minimum of the spinodal curve a in Fig. 1). Figure 2A presents the gray scale images of the evolution at increasing times (images A1−A10 from left to right), and Fig. 2B displays selected 3-D images of the same evolution (images B1−B4). The hatched areas in Fig. 2A and all of the subsequent figures denote a largely flat film of equilibrium thickness corresponding to the secondary minimum in the free energy per unit area curve (pseudo-dewetting). The initial random disturbance first transforms into a bicontinuous structure composed of uneven long hills and valleys, which then evolves into small-amplitude circular depressions and liquid ridges (images A2 and B1 in Fig. 2). Fragmentation of ridges directly produces increasingly circular droplets which become increasingly isolated by the coalescence and thinning of valleys surrounding them (image A3). The first signs of pseudo-dewetting appear *after* the formation of droplets (hatched areas in images A4 and B2). At this stage, droplets grow both by continued thinning of valleys, which increases the dewetted area, and by merger or ripening, which is driven by the flow from smaller to larger droplets due to Laplace pressure gradients (images A5−A7). After dewetting is complete, further evolution occurs only by the ripening of the structure in which larger drops grow at the expense of smaller ones, thus decreasing the number density of drops (images A7−A10 and images B2−B4). Eventually, a truly thermodynamic stable state is reached, which is represented by the co-existence of a single drop (image A10) with its surrounding equilibrium flat thin film, which may be called the situation of 'pseudo-partial wetting'. Thus, for films thinner than the secondary minimum in the spinodal parameter, the onset of dewetting by the formation of a contact line occurs *after* the formation of isolated, mature circular droplets. Droplets are formed directly by the fragmentation of an initially bicontinuously undulating structure.

Figure 3 shows the fractional area covered by the liquid regions above the mean thickness (curve a) and above a cut-off equilibrium thickness (curve b) for the 7 nm film of Fig. 2 (the equilibrium cut-off thickness was defined as 15% thicker than the final minimum equilibrium thickness at long times). The fractional dewetted
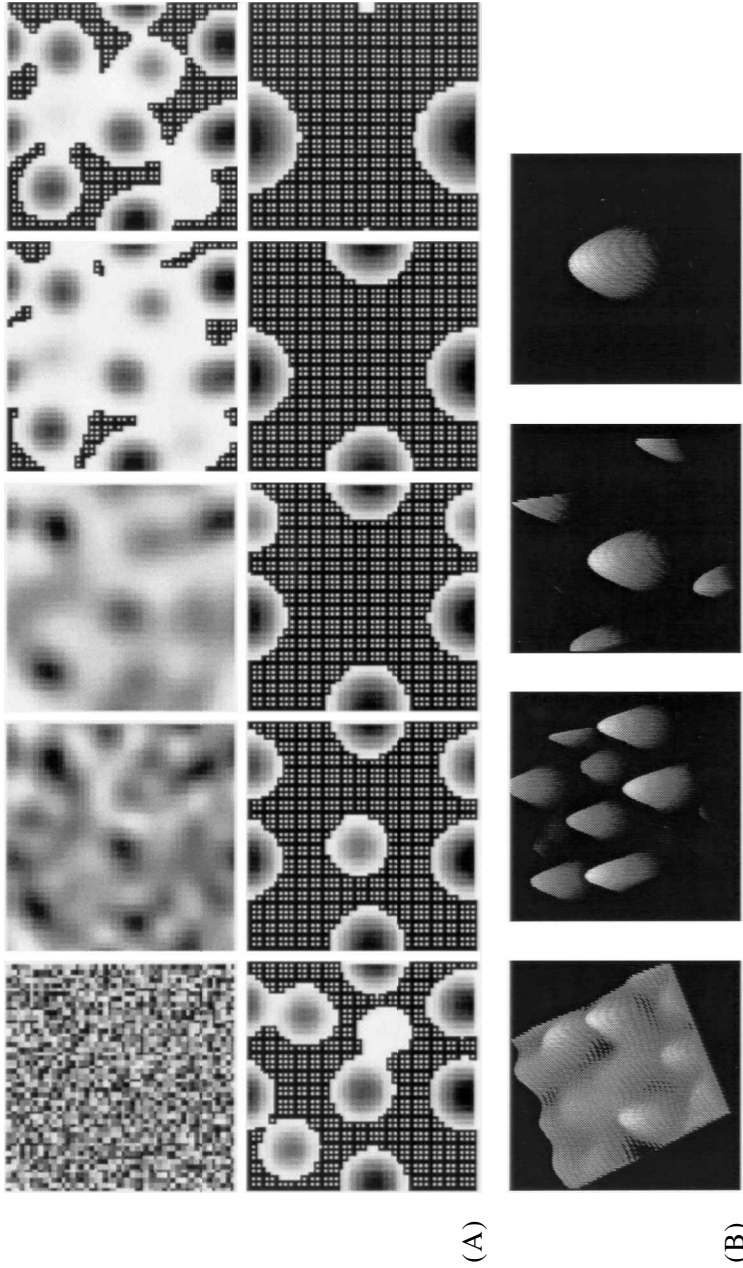
(A)

(B)

Figure 2. Different stages of the evolution of a 7 nm thick film, which is thinner than the location of the minimum (at 7.82 nm) in the spinodal parameter vs. thickness curve a of Fig. 1. The area of each cell is $9L^2$ (nondimensional wavelength $L = 17.24$). Series A: continuous shading is employed between the minimum and maximum thicknesses in each image. The hatched regions represent the pseudo-dewetted areas. The onset of dewetting is clearly seen in image A4 (from left to right, top). Gray scale images in the two rows correspond to (from left to right): $T = 0, 8, 91, 206, 241, 362, 859, 1455, 2004,$ and 7124, respectively. The corresponding nondimensional maximum and minimum thicknesses (H) in images 1 to 10 are (1.099, 0.9), (1.03, 0.97), (1.13, 0.94), (1.98, 0.82), (2.1, 0.81), (2.3, 0.79), (2.73, 0.78), (3.03, 0.78), (3.26, 0.77), and (4.04, 0.77), respectively. Series B: 3-D morphologies of the film are shown at $T = 92, 242, 4453$ and 7123, respectively.
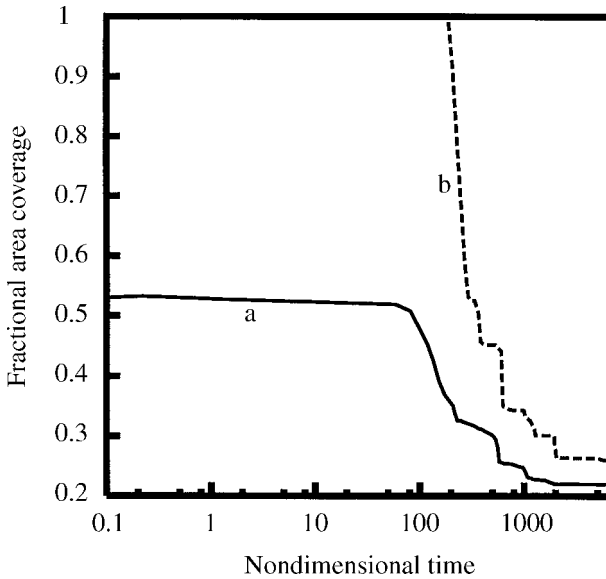
Figure 3. Fractional area coverage by the liquid regions thicker than the threshold thickness. Variations of the fractional coverage above the mean thickness (curve a) and above 15% of the equilibrium thickness (curve b) with the nondimensional time are shown for a 7 nm film.

area is simply $1-$ fractional area coverage in curve b. Inspection of curve b shows that after the onset of dewetting (at nondimensional time $T \approx 200$), the dewetted area increases almost linearly until the process of ripening becomes important (at $T \approx 300$); thereafter, the dewetted area increases in discrete steps which mirror the disappearance of smaller drops by ripening. Similarly, curve a shows a rapid decline in the area occupied by the liquid ridges/droplets above the mean film thickness until the onset of dewetting, and a slower decline thereafter. The initial rapid decline is due to the fragmentation of ridges to produce more compact circular droplets of increased heights. After the onset of dewetting, slower changes occur due to retraction of droplets making them more circular and compact ($T < 600$), and thereafter by ripening.

Figure 4 for the 7 nm film of Fig. 2 quantifies the lateral extent and amplitude of depressions (valleys or regions below the mean thickness), as well as the amplitude of ridges (regions above the mean thickness). A convenient way to quantify the lateral extent is the effective mean radius, defined as twice the area covered by depressions divided by the total perimeter of depressions. In the first phase ($T < 80$), there is only a rearrangement leading to a bicontinuous pattern. Depressions merely widen slowly without becoming deeper. The minimum thickness then declines, leading to the onset of dewetting ($T \approx 200$), by which time droplets have emerged (the maximum nondimensional thickness increases to about 2). After dewetting begins, the effective radius of depressions grows with time almost as $\log(T)$. Figure 4 also clearly points out that in relatively thin films, a significant
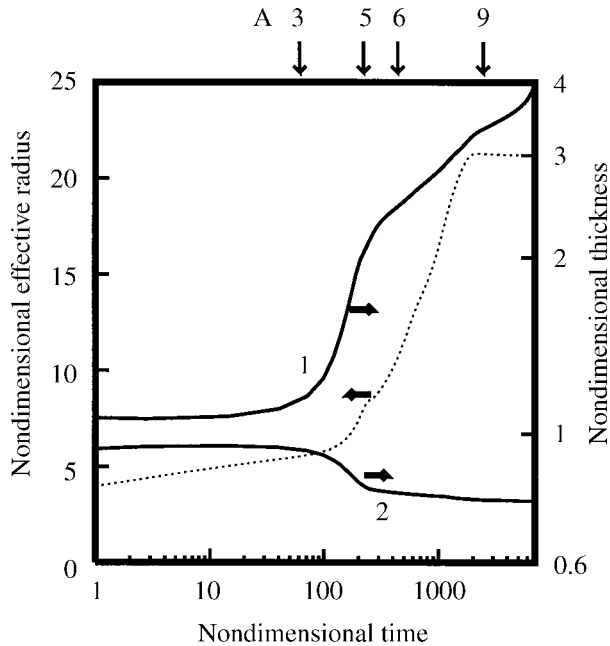
Figure 4. Variations of the nondimensional effective radius of depressions (below the mean thickness), maximum thickness (curve 1), and minimum thickness (curve 2) for a 7 nm film. The arrows numbered 3, 5, 6, and 9 on top indicate the times corresponding to images 3, 5, 6, and 9 of series A in Fig. 2.

growth of depressions leading to dewetting is concluded only after the formation of droplets, which continue to grow further by ripening, but with different kinetics.

The same qualitative pathway of morphological evolution was seen in a large number of simulations (not shown) for all thicknesses to the left of the minimum in the $\partial^2 \Delta G / \partial h^2$ vs. thickness curve, regardless of the numerical values of the parameters A, S^P and l_p which characterize the potential.

In contrast to the above scenario, Fig. 5 shows a different pattern of self-organization and a different pathway of dewetting for a thick film (25 nm), which is much thicker than the thickness at which the minimum in the spinodal parameter occurs (Fig. 1). The initial random disturbances (image A1 in Fig. 5) are again first organized into a small-amplitude bicontinuous pattern on a length scale close to the dominant wavelength calculated from the linear stability analysis (image A2). Thereafter, largely circular depressions emerge and quickly grow into full thickness isolated holes which initiate dewetting (images A3, A4, B1, and B2). New holes continue to form, expand, and coalesce thereafter (images A5–A8, B3, and B4). The axisymmetry of the holes is gradually lost because of the interaction with neighboring holes. A large-scale structure of liquid ridges and dewetted areas forms by repeated coalescence of holes (image A9), which then transforms into droplets by fragmentation of ridges, which is reminiscent of the Rayleigh instability (images A10 and B5).
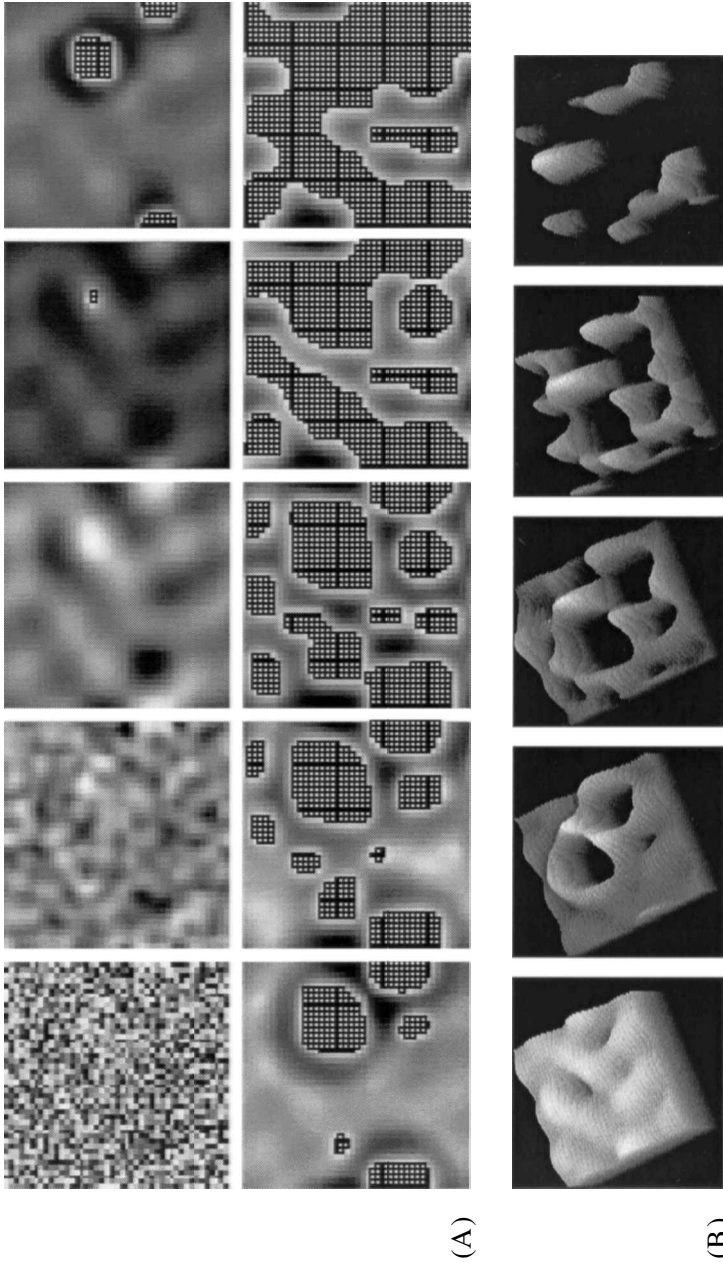
(A)

(B)

Figure 5. Different stages of evolution in a 25 nm thick film, which is much thicker than the location of the minimum (at 7.82 nm) in the spinodal parameter vs. thickness curve a of Fig. 1. The area of each box is $9L^2 (L = 8.9)$. Series A: gray scale images correspond to (from left to right) $T = 0, 0.06, 5.16, 8.8, 10.2, 12.0, 13.5, 15.5, 20.4,$ and 1687, respectively. The onset of dewetting can be clearly seen in image A4. The corresponding nondimensional maximum and minimum thicknesses (H) in images 1–10 are (1.09, 0.9), (1.05, 0.94), (1.09, 0.89), (1.17, 0.22), (1.44, 0.206), (2.08, 0.205), (2.64, 0.204), (2.83, 0.204), (4.07, 2.05), and (5.39, 0.205), respectively. The nondimensional equilibrium thickness is 0.2. Series B: 3-D morphologies are shown at $T = 8.8, 11.7, 13.5, 15.5,$ and 1687.
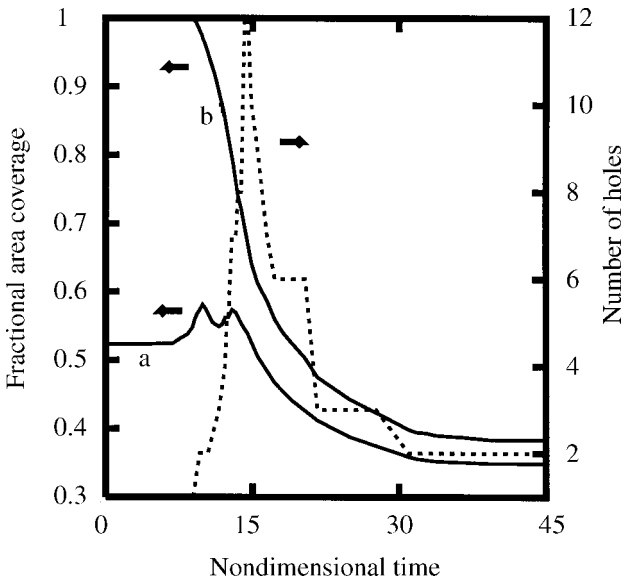
Figure 6. Fractional area coverage by the liquid regions thicker than the threshold thickness. Variations of the fractional coverage above the mean thickness (curve a) and above 15% of the equilibrium thickness (curve b) with the nondimensional time are shown for a 25 nm film. The number of holes is shown by the dotted curve.

Figure 6 shows the fractional area covered by the liquid regions above the mean thickness (curve a), and above the cut-off equilibrium thickness (curve b), during the course of evolution for the 25 nm thick film. The same figure also gives information on the temporal evolution of the number of holes, which initially increase and then decline due to coalescence. The area still covered by the liquid declines sharply during the hole formation and growth ($T < 15$) and more slowly thereafter. The area covered by ridges above the mean thickness (curve a) increases slightly after the formation of rims around the holes, but starts to decline after the hole coalescence dominates ($T > 15$). A slight intermediate oscillation is due to a composite effect of the two concurrent processes of hole growth and hole coalescence.

Figure 7 (to be contrasted with Fig. 4) presents the effective radius of depressions and the minimum and maximum thicknesses for the 25 nm film. In the first phase ($T < 7$), there is a significant widening of depressions without a concurrent change in amplitudes. Rupture by holes occurs rather explosively, without a significant increase in the maximum thickness during the hole formation. The appearance of new holes decreases the radius slightly. The continued hole expansion and dewetting, however, lead to a sustained growth of the effective radius at long times.

A very similar sequence of morphological evolution (bicontinuous pattern $\rightarrow$ circular holes with rims $\rightarrow$ hole expansion $\rightarrow$ hole coalescence) was also shown [24–26] by simulations in the following two general classes of systems: (a) films subject only to a long-range van der Waals attraction, regardless of their mean thickness; and (b) relatively thick, type IV films close to their upper spinodal
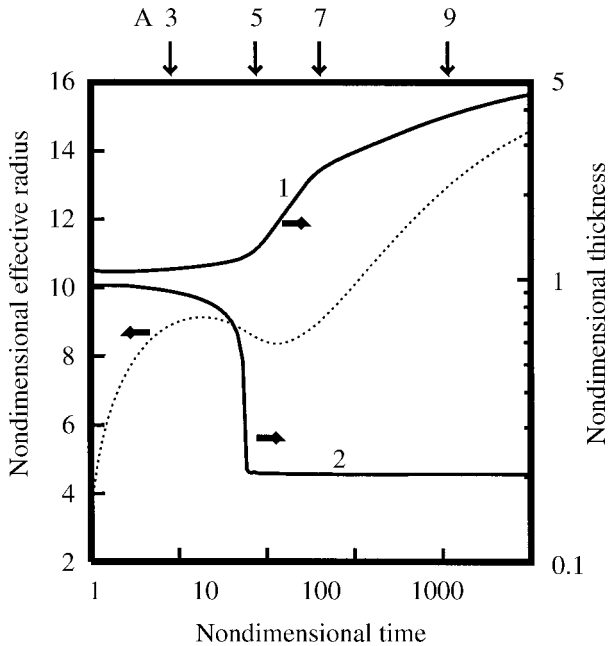
Figure 7. Variations of the nondimensional effective radius of depressions (below the mean thickness), the maximum thickness (curve 1), and the minimum thickness (curve 2) with time for a 25 nm thick film. The arrows numbered 3, 5, 7, and 9 on top indicate the times corresponding to images 3, 5, 7, and 9 of series A in Fig. 5.

boundary. In the latter system, the spinodal (unstable) region occurs in the vicinity of the primary minimum, which is different from the case considered here. The present study thus reinforces the belief in a general pathway of pattern evolution and dewetting by the formation of isolated holes whenever the initial mean thickness is sufficiently high so that the repulsive interactions at the minimum thickness are encountered only after a considerable growth of the instability. This conclusion appears to be independent even of the general classes of the potential, namely it seems to hold for all combinations of attractive and repulsive, and of short- and long-range forces. The formation of circular holes is therefore not always indicative of 'nucleation' by large dust particles, defects, etc., but can also occur by a spontaneous growth of surface instability as the film thickness increases towards the upper spinodal boundary (for the type II system, the upper spinodal is at infinity).

Figure 8 shows the evolution for an intermediate thickness film (10 nm in Fig. 1). The initial bicontinuous pattern resolves into a mixture of both drops and depressions displaying less axisymmetry in varying proportions (image 1). Dewetting still occurs by the formation of holes, which now all appear within a narrower window of time compared with thicker films. Coalescence of holes produces a bicontinuous dewetted structure made up of long ridges and flat valleys. Ridges disintegrate to produce the droplets.
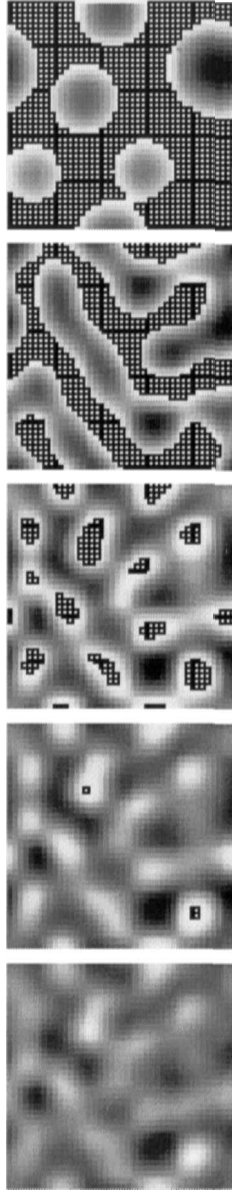
Figure 8. Evolution of the pattern in an intermediate thickness film (10 nm). The area of each box is $16L^2$ ($L = 9.27$). The onset of dewetting can be clearly seen in the second image. The gray scale images correspond to (from left to right) $T = 9$, 15, 19, 35, and 435, respectively. The corresponding nondimensional maximum and minimum thicknesses (H) are (1.15, 0.81), (1.4, 0.57), (1.69, 0.53), and (3.78, 0.52), respectively.
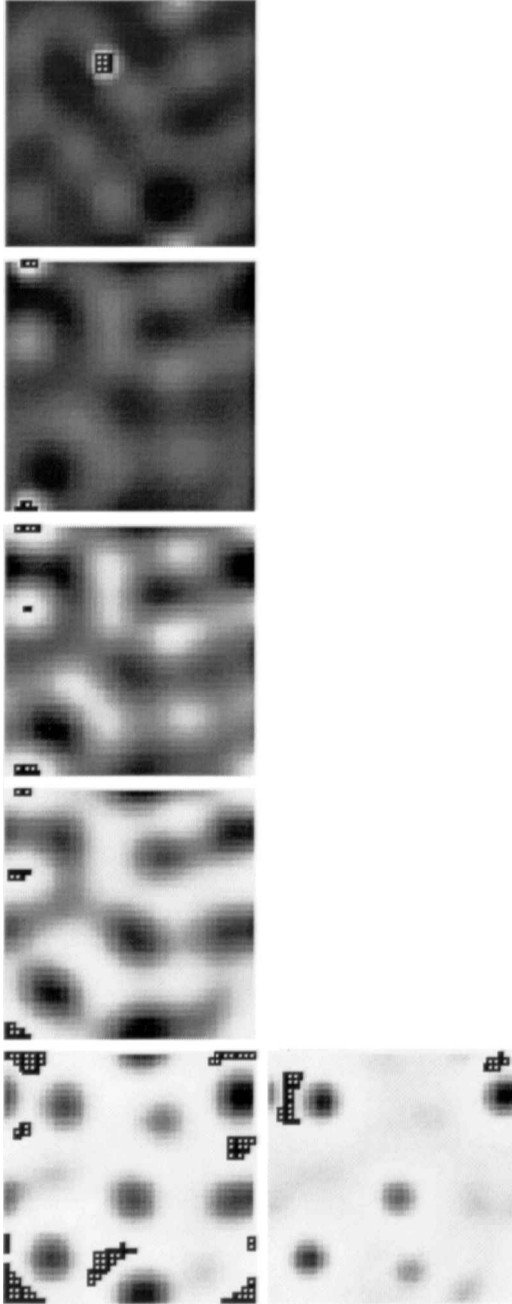
Figure 9. Morphology at the onset of dewetting in 7 nm, 8 nm, 10 nm, 15 nm, and 25 nm thick films of the system represented by curve a in Fig. 1. For a different potential (curve b), the lone image in the next row represents the pattern at the onset of dewetting in a 10 nm film. The areas shown are $9L^2$. A continuous linear gray scale between the minimum and the maximum thicknesses in each image is used.

Thus, different pathways of pattern evolution can produce strikingly different morphologies at the onset of dewetting in films of different thicknesses as summarized clearly in Fig. 9. For a 7 nm film, dewetting occurs by the formation of circular droplets. For intermediate thickness, slightly to the right of the spinodal minimum, a bicontinuous pattern of ridges and valleys exists at the onset of dewetting, the structure being more uniform and connected for thicker films. At still higher thickness (15 and 25 nm), dewetting occurs by isolated holes which become increasingly circular for thicker films.

The morphological pathway of dewetting thus depends only on the relative location of the film thickness *vis-à-vis* the location of the minimum in the spinodal parameter. Figure 9 further illustrates this point in the last image, which shows the pattern at the time of dewetting for a 10 nm film of a different system represented by curve b of Fig. 1, where the minimum occurs at 12 nm. Dewetting indeed occurs by droplets, rather than by a bicontinuous structure. Thus, as far as the qualitative morphological features are concerned, a 10 nm thick film of a system displaying the spinodal minimum at 12 nm is similar to a 7 nm film of a system with the spinodal minimum at 8 nm. Thus, the pattern is governed not by the film thickness *per se*, but by its positioning *vis-à-vis* the location of the spinodal minimum, which is different for different systems.

Recent experiments of Herminghaus *et al.* [18] with thin liquid crystal films show the same qualitative variation of the free energy as used in the simulations here. The most prominent feature is the existence of a primary and a secondary minimum. Interestingly, films close to the secondary minimum showed two distinct, but co-existing, patterns and pathways of dewetting [18]: (a) pseudo-dewetting in the secondary minimum by a correlated undulating structure similar to the one seen in simulations for relatively thin to moderate thickness films (Figs 4, 8, and 11) before the long-term formation of circular drops, and (b) true dewetting in the primary minimum by the formation of randomly distributed circular holes. Based on our simulations, we hypothesize that the latter structure results from the heterogeneity of the substrate in conjunction, possibly, with the heterogeneity of the molecular ordering close to the substrate surface, which leads to a weaker short-range repulsion and therefore a shift of the secondary minimum to a smaller thickness closer to the primary minimum. On such randomly distributed patches, pseudo-dewetting should occur by the formation of circular holes since the distance between the (secondary) spinodal minimum and the film thickness increases. The equilibrium film left at the base also becomes much thinner so that 'nucleation' to the primary minimum now becomes easier. Indeed, in another set of experiments with molten gold films [18], which do not experience a soft repulsion, correlated holes could be witnessed. This is in conformity with the simulations reported here and those published previously for purely attractive long-range forces [24]. In experiments on aqueous films on graphite [17] and on low-molecular-weight polystyrene films [11] on silicon (both of which are type IV systems considered elsewhere [25, 26]), holes due to both nucleation and spinodal dewetting seem

to co-exist. For aqueous films, the population of holes produced by the spinodal mechanism is expected to increase with increased rate of evaporation [35], as evidenced also in the experiments [17].

Simulations show that the magnitude of the characteristic length scale of the instability is well predicted by the linear analysis of the dominant wavelength *until the onset of dewetting*. For example, a maximum of eight droplets and 12 holes appear in Figs 2 and 5 (see also Fig. 6), respectively. Since these simulations are carried out over an area of $9L^2$, the linear theory would anticipate nine structures. The hole density was almost always found to be slightly larger, since additional holes at late times continue to form in the interstitial spaces whenever the space available is larger than the critical length. It is well known that the critical wavelength for the instability is smaller by a factor of $\sqrt{2}$ than the dominant wavelength of the linear theory. Of course, at late times, the structure coarsens due to hole coalescence or by ripening of drops, and the length scale of the structure can no longer be predicted by the linear theory.

Finally, we consider the Minkowski functional for the connectivity of patterns [38, 39], which is a useful topological measure used for the analysis of thin films [13, 18] and other patterns [38]. To analyze the connectivity of a pattern, a two-color representation of the film morphology is first formed by dividing the regions above (black) and below (gray) a threshold thickness. We chose the mean film thickness to threshold the image in order to facilitate convenient comparisons with future experimental work. The connectivity is simply a measure of the difference between the number of isolated (disconnected) gray domains (G) and the number of isolated black domains (B). The normalized connectivity is $[(G - B)/(G + B)]$. Connectivity is positive (negative) if the number of isolated depressions is larger (smaller) than the number of distinct ridges. The connectivity measure is also an indicator of the mean curvature of the pattern [37], positive (negative) connectivity implying the dominance of concave (convex) black regions. Thus, the presence of isolated holes (droplets) leads to a positive (negative) connectivity. Connectivity vanishes when the numbers of black and gray domains are equal. The evolution of connectivity with time also gives a clue regarding whether the pattern is correlated (e.g. arising through a spinodal mechanism) or random (e.g. a Poissonian process) [13]. Further details regarding computations of connectivity from the gray scale images (or profiles) are given elsewhere [38, 39].

Figure 10 shows the temporal evolution of connectivity for 7 nm, 10 nm, and 25 nm thick films. Typical two-color representations of the morphology for 7 nm (droplet forming) and 25 nm (hole-forming) films are summarized in Figs 11 and 12, respectively. For the 7 nm film, connectivity is initially negative since the initial rearrangement produces a structure in which the number of isolated ridges exceeds the number of isolated valleys (image 1 in Fig. 11). The isolated hills coalesce to form longer interconnected ridges, some of which trap isolated depressions (image 2 in Fig. 11). Connectivity now becomes positive. Further evolution produces a bicontinuous pattern where both the ridges and the valleys are equally connected
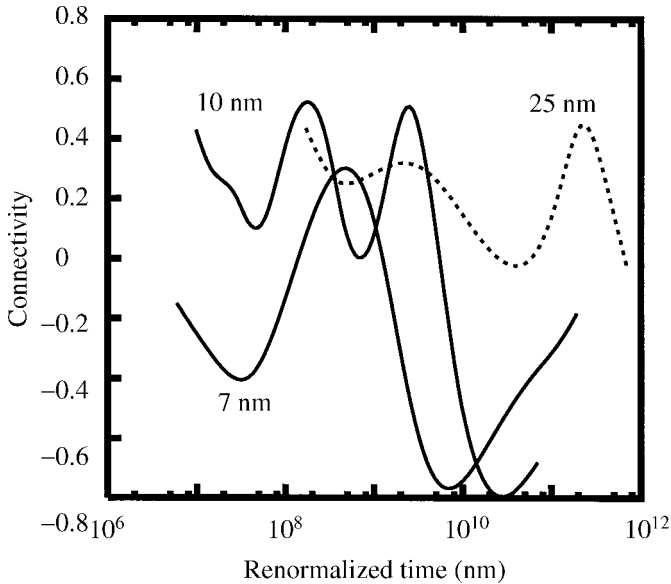
Figure 10. Connectivity of the pattern at a threshold thickness equal to the mean film thickness for 7 nm, 10 nm, and 25 nm thick films. A scaled renormalized time, t_N (in nm) $= Th(h/d_0)^4$, as defined in the text, is used ($d_0 = 0.158$ nm).

(image 3 in Fig. 11), and the connectivity thus once again passes through zero. Fragmentation of ridges into droplets leads to negative connectivity (image 4), and finally, at late times, ripening (image 5) increases connectivity due to decreased drop density.

In contrast to the above scenario, connectivity for a thick hole forming 25 nm thick film remains positive at all stages of evolution and dewetting except at very long times after the conclusion of coalescence leading to droplet formation (not shown). Connectivity initially declines (image 1 in Fig. 12) until a bicontinuous pattern is formed (image 2 in Fig. 12). The formation of isolated depressions developing into holes (image 3 in Fig. 12) increases the connectivity until a maximum is reached after some coalescence (image 4). Thereafter, the fragmentation of ridges starts to produce isolated (noncircular) droplets, which decreases the connectivity. Further evolution would have produced an array of droplets (not shown), leading to negative connectivity.

The connectivity features for intermediate thickness (e.g. curve for 10 nm in Fig. 10) are more complex, but are clearly derived from a combination of the characteristics of thin and thick films. In general, if one considers the evolution *until dewetting*, the regions showing positive (negative) connectivity enlarge (shrink) as the film gets thicker. In fact, for films thicker than the critical thickness, connectivity always remains positive. Thus, the connectivity measure appears to be a useful tool for characterizing and discriminating the thin film patterns and their pathways of
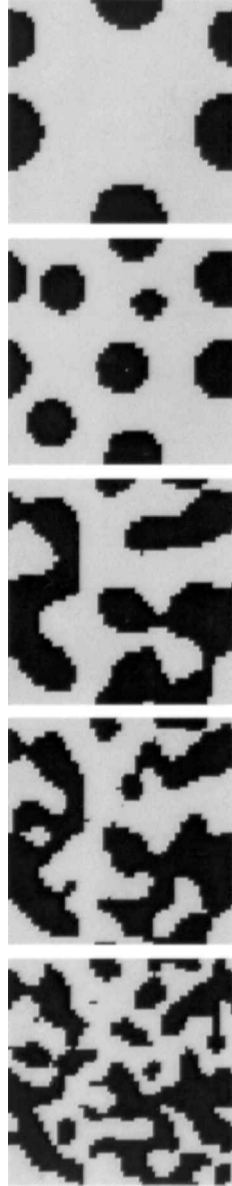
Figure 11. Two-color representation of the film morphology in a 7 nm thick film. Black and gray represent the regions above and below the mean thickness, respectively. The images correspond to (from left to right) $t_N(\times 10^{-7}) = 4.12, 23, 159, 816,$ and 3230 nm, respectively. t_N is as defined in Fig. 10.

Figure 12. Two-color representation of the film morphology in a 25 nm thick film. Black and gray represent the regions above and below the mean thickness, respectively. The images correspond to (from left to right) $t_N (\times 10^{-9}) = 1.6, 100, 180, 280,$ and 600 nm, respectively. t_N is as defined in Fig. 10.

evolution, especially from experiments. The theory presented here will be useful for this purpose.

Interestingly, it may be noted that two-color representations of the morphology (e.g. Figs 11 and 12), which are often used to depict experimental morphologies, carry much less information than their gray scale counterparts. In fact, mere visual observation of Figs 11 and 12 does not readily suggest the rather drastic differences in the pathways of evolution evidenced in the detailed gray scale images (the formation of droplets in Fig. 12 at long times is not shown, the addition of which would make it almost identical to Fig. 11). Moreover, patterns can be made to appear different by choosing a different threshold thickness in the two-color representations. A more complete analysis of an experimental pattern requires computations of connectivity at different threshold thicknesses [26, 38]. This would facilitate a more meaningful comparison between simulations and experiments.

4. CONCLUSIONS

The morphological pathways of spontaneous pattern evolution and dewetting have been studied in type II films in the spinodal region around the secondary minimum of the spinodal parameter, which is the negative curvature of the excess free energy per unit area. Relatively thick films some distance away to the right of the spinodal minimum are dewetted by the formation of isolated circular holes, which grow and coalesce to form a giant structure of liquid ridges, which in turn decays into droplets. In thick films, not all holes appear within a narrow window of time, as may be concluded from the linear analysis. Droplets are formed at an increasingly earlier stage of evolution as the film thickness decreases. Films thinner than the spinodal minimum decay into droplets via a bicontinuous structure before the onset of dewetting. An important conclusion is that different morphologies (isolated circular holes, droplets, bicontinuous) and their combinations can all be produced depending on the film thickness *vis-à-vis* the location of the minimum in the force vs. thickness curve. Moreover, all three patterns (holes and drops of varying sizes, bicontinuous ridges, and droplets) can co-exist in varying proportions at a given time even on homogeneous surfaces, especially for intermediate thickness films. Since most real (and even experimental) surfaces are heterogeneous, they can support a wide variety of patterns resulting from the spinodal dewetting alone. The results presented here are also germane to films displaying many local spinodal minima due to layering, as the evolution in each local minimum is governed by the same considerations.

Regardless of the morphology, however, the structure is correlated, and its length scale is adequately predicted by the linear analysis *until the onset of dewetting*. Hole coalescence or droplet ripening produces larger-scale structures at late times after dewetting. However, it can be noted that on a heterogeneous surface, large-scale correlation of the structure may be lost, but the local morphology will still be governed by the local potential.

The above results should aid our understanding, design, and interpretation of thin film experiments, where the linear analysis has hitherto been used as the guide.

REFERENCES

1. A. Vrij, *Discuss. Faraday Soc.* **42**, 23 (1966).
2. E. Ruckenstein and R. K. Jain, *J. Chem. Soc., Faraday Trans. 2* **70**, 132 (1974).
3. B. V. Derjaguin, *Theory of Stability of Thin Films and Colloids.* Consultants Bureau / Plenum Press, New York (1989).
4. A. Sharma, *Langmuir* **9**, 861 (1993).
5. G. Reiter, *Phys. Rev. Lett.* **68**, 75 (1992).
6. G. Reiter, *Langmuir* **9**, 1344 (1993).
7. G. Reiter, P. Auroy and L. Auvray, *Macromolecules* **29**, 2150 (1996).
8. W. Zhao, M. H. Rafailovich, J. Sokolov, L. J. Fetters, R. Plano, M. K. Sanyal, S. K. Sinha and B. B. Sauer, *Phys. Rev. Lett.* **70**, 1453 (1993).
9. J. M. Guerra, M. Srinivasrao and R. S. Stein, *Science* **262**, 1395 (1993).
10. L. Sung, A. Karim, J. F. Douglas and C. C. Han, *Phys. Rev. Lett.* **76**, 4368 (1996).
11. R. Xie, A. Karim, J. F. Douglas, C. C. Han and R. A. Weiss, *Phys. Rev. Lett.* **81**, 1251 (1998).
12. J. Bischof, D. Scherer, S. Herminghaus and P. Leiderer, *Phys. Rev. Lett.* **77**, 1536 (1996).
13. K. Jacobs, S. Herminghaus and K. R. Mecke, *Langmuir* **14**, 965 (1998).
14. G. Reiter, A. Sharma, R. Khanna, A. Casoli and M.-O. David, *J. Colloid Interface Sci.* **214**, 126–128 (1999).
15. G. Reiter, A. Sharma, R. Khanna, A. Casoli and M.-O. David, *Europhys. Lett.* **46**, 512–518 (1999).
16. G. Reiter, A. Sharma, A. Casoli, M.-O. David, R. Khanna and P. Auroy, *Langmuir* **15**, 2551–2558 (1999).
17. U. Thiele, M. Mertig and W. Pompe, *Phys. Rev. Lett.* **80**, 2869 (1998).
18. S. Herminghaus, K. Jacobs, K. Mecke, J. Bischof, A. Fery, M. Ibn-Elhaj and S. Schlagowski, *Science* **282**, 916 (1998).
19. M. B. Williams and S. H. Davis, *J. Colloid Interface Sci.* **90**, 220 (1982).
20. A. Sharma and A. T. Jameel, *J. Colloid Interface Sci.* **161**, 190 (1993).
21. A. Sharma and A. T. Jameel, *J. Chem. Soc., Faraday Trans.* **90**, 625 (1994).
22. R. Khanna, A. T. Jameel and A. Sharma, *Ind. Eng. Chem. Res.* **35**, 3108 (1996).
23. A. Sharma and G. Reiter, *J. Colloid Interface Sci.* **178**, 383 (1996).
24. R. Khanna and A. Sharma, *J. Colloid Interface Sci.* **195**, 42 (1997).
25. A. Sharma and R. Khanna, *Phys. Rev. Lett.* **81**, 3463 (1998).
26. A. Sharma and R. Khanna, *J. Chem. Phys.* **110**, 4929 (1999).
27. J. W. Cahn, *J. Chem. Phys.* **42**, 93 (1965).
28. J. N. Israelachvili, *Intermolecular and Surface Forces.* Academic Press, London (1992).
29. C. J. van Oss, M. K. Chaudhury and R. J. Good, *Chem. Rev.* **88**, 927 (1988).
30. K. R. Shull, *J. Chem. Phys.* **94**, 5723 (1991).

31. K. R. Shull, *Faraday Discuss.* **98**, 203 (1994).
32. X. L. Chu, A. D. Nikolov and D. T. Wasan, *J. Chem. Phys.* **103**, 6653 (1995).
33. V. Bergeron and C. J. Radke, *Langmuir* **8**, 3020 (1992).
34. H. Riegler, A. Asmussen, M. Christoph and A. Davydov, in: *Proceedings of 30th Rencontres de Moriond, Short and Long Chains at Interfaces*, J. Daillant, P. Guenoun, C. Marques, P. Muller and J. T. T. Van (Eds), pp. 307–312. Editions Frontieres, Gif-sur-Yvette, France (1995).
35. A. Sharma, *Langmuir* **14**, 4915 (1998).
36. N. N. Yanenko, *The Method of Fractional Steps*. Springer-Verlag, New York (1971).
37. D. A. Anderson, J. C. Tannehill and R. H. Pletcher, *Computational Fluid Mechanics and Heat Transfer*. Hemisphere, Washington, DC (1984).
38. K. R. Mecke, *Phys. Rev. E* **53**, 4794 (1996).
39. A. Rosenfield and A. C. Kak, *Digital Picture Processing.* Academic Press, New York (1976).